Global warming accelerates soil heterotrophic respiration

Alon Nissan (anissan@ethz.ch)
ETH Zürich https://orcid.org/0000-0003-1300-5591
Uria Alcolombri
ETH Zurich https://orcid.org/0000-0003-3561-5091
Nadav Peleg
University of Lausanne https://orcid.org/0000-0001-6863-2934
Nir Galili
ETH Zürich
Joaquin Jimenez-Martinez
Swiss Federal Institute of Aquatic Science and Technology https://orcid.org/0000-0002-2063-6490
Peter Molnar
ETH Zurich https://orcid.org/0000-0001-6437-4931
Markus Holzner
WSL, Birmensdorf,

Article

Keywords: Soil heterotrophic respiration, carbon cycle, soil micro-scale processes, global warming, soil-climate respiration model, past and future soil respiration trends

Posted Date: October 6th, 2022

DOI: https://doi.org/10.21203/rs.3.rs-1937650/v1

Global warming accelerates soil heterotrophic respiration

Alon Nissan[1*], Uria Alcolombri[1], Nadav Peleg[2], Nir Galili[3], Joaquin Jimenez-Martinez[1,4], Peter Molnar[1] and Markus Holzner[4,5]

[1]Institute of Environmental Engineering, Department of Civil, Environmental and Geomatic Engineering, ETH Zürich, Zürich, 8093, Switzerland.
[2]Institute of Earth Surface Dynamics, University of Lausanne, Lausanne, 1015, Switzerland.
[3]Geological Institute, Department of Earth Sciences, ETH Zürich, Zürich, 8092, Switzerland.
[4]Department of Water Resources and Drinking Water, Swiss Federal Institute of Aquatic Science and Technology, EAWAG, Dübendorf, 8600, Switzerland.
[5]Biodiversity and Conservation Biology, Swiss Federal Institute for Forest Snow and Landscape Research, WSL, Birmensdorf, 8903, Switzerland.

*Corresponding author(s). E-mail(s): anissan@ethz.ch;
Contributing authors: alcolombri@ifu.baug.ethz.ch; nadav.peleg@unil.ch; ngalili@ethz.ch; joaquin.jimenez@eawag.ch; peter.molnar@ifu.baug.ethz.ch; markus.holzner@wsl.ch;

Abstract

Carbon efflux from soils is the largest terrestrial carbon source to the atmosphere, yet it remains one of the most uncertain fluxes in the Earth's carbon budget. A dominant component of this flux is heterotrophic respiration, influenced by several environmental factors, most notably soil temperature and moisture. We developed a mechanistic model from micro to global scale to explore how changes in soil water content and temperature affect soil heterotrophic respiration. Simulations, laboratory measurements, and field observations validate the new approach. Estimates from the model show that heterotrophic respiration has been increasing since the 1980s at a rate of about 1.7% per decade globally. Using future projections of surface temperature and soil moisture, the model predicts a global increase of about 40% in heterotrophic respiration by the end of the century under the worst-case emission scenario, which is driven principally by the reduction of soil moisture rather than temperature increase.

Keywords: Soil heterotrophic respiration, carbon cycle, soil micro-scale processes, global warming, soil-climate respiration model, past and future soil respiration trends

1 Introduction

Rising atmospheric carbon dioxide (CO_2) concentration is one of the primary contributors to global warming [1]. Within the terrestrial carbon cycle, soil respiration, the emission of CO_2 through root (autotrophic) and microbial (heterotrophic) respiration, is the largest carbon efflux into the atmosphere [1, 2]. Therefore, reliable quantification of how soil respiration may be affected by climate change is critical for predicting future atmospheric CO_2 concentrations. Although terrestrial carbon fluxes play a key role in the global carbon budget, their current estimates are highly uncertain [3–5]. Soil carbon fluxes are dependent on complex interactions between biological, chemical, and physical processes, played out under fluctuating and heterogeneous environmental conditions, making them difficult to measure and model.

Soils play a vital role in transferring, buffering, filtering, and accumulating carbon at the interface between the atmosphere, biosphere, and lithosphere. For example, soils contain about three times as much carbon (1500–2400 PgC, $1\ \text{Pg} = 10^{15}\ \text{g}$) as the atmosphere (600–800 PgC) or the Earth's vegetation (450–650 PgC) [1, 6]. Roughly a quarter of atmospheric CO_2 originates from soils [7], which is five times more than anthropogenic CO_2 emissions [8]. Soil heterotrophic respiration (HR) is one of the primary mechanisms through which terrestrial ecosystems release CO_2 into the atmosphere, and its relative contribution has been observed to gradually increase over the past two decades [9]. HR varies over a wide range of time scales (e.g., daily fluctuations and seasonal cycles), and is principally controlled by two climatic variables: soil temperature and moisture [8]. While the soil temperature is positively correlated with HR [10, 11], soil moisture shows a non-monotonic relationship [12]. Low soil moisture content reduces HR rates by limiting solute flux due to poor water connectivity in the pores. High moisture content reduces HR by limiting oxygen (O_2) supply from the atmosphere due to the weak diffusivity of O_2 in water relative to gas. As a result, the response of HR to soil water saturation shows a bell-shaped response curve, with optimal conditions for respiration at intermediate soil moisture content.

Modelling HR rates based on soil temperature and moisture is challenging due to the many interacting processes that are controlled by these variables [8, 13]. Consequently, most modelling efforts to quantify changes in HR rates as a function of temperature and moisture employ empirical parameterizations using macro-scale (bulk) properties of the soil (e.g., [14, 15]) or empirical fits using a variety of function shapes (e.g., [13, 16, 17]). These parameterizations often have no direct connection to biophysical processes, and are site dependent rather than universal laws [13].

Here, we provide a mechanistic perspective on soil HR built upon pore-scale processes at the grain interface where microbial communities reside (see inset of Fig. 1 as representation), and link this to global-scale patterns and future trends. We first quantified soil HR starting from the pore (micro) scale, integrating parameters that are biological (e.g., microbial respiration and production of CO_2), chemical (reaction processes), and physical (transport mechanisms and soil texture). Subsequently, we upscaled the pore-scale HR relations by defining scaling laws from pores to water patches using percolation theory [18], which allows us to make predictions of HR fluxes for larger (continuum) scales while maintaining the biophysical representation of the pore scale. Then, considering soil temperature and moisture variation in space and time, we show that the model yields estimates of recent trends in soil HR rates at the global scale that are in line with observations. Finally, we use this mechanistic model to simulate how soil HR might change under the worst-case future climate scenario from CMIP6 climate change experiments.

2 Results

2.1 Soil heterotrophic respiration at the pore scale

To quantify the non-linear relationship between HR and soil moisture content [12], which is considered to be the most uncertain parameter when estimating soil HR [13], we started by performing pore-scale numerical simulations using an image-based percolation algorithm, to obtain the air–water distribution in the soil matrix under different saturation degrees [19] (Methods and Extended data Fig. 1a). Different soil configurations were examined by changing the characteristic grain diameter λ_c. The soil configurations were generated using a random distribution of circular grains with radius λ_c.

Based on the air–water distribution in the soil from the percolation simulations (Extended data Fig. 1b), reactive transport simulations were computed on the 2D pore-scale domains [20] (Methods and Fig. 1) to quantify the response of HR to soil saturation degree ($\tilde{\theta} = \theta/\theta_s$, where θ_s is the moisture capacity of the porous media). In these simulations, other environmental conditions (e.g., ambient temperature and reaction parameters) were kept constant (Extended data Table 1). The inset in Fig. 2a shows the model output, revealing the expected non-monotonic relationship between $\tilde{\theta}$ and mean soil HR, $\tilde{R_h} = \int_\Omega \frac{R_h}{V_m} d\Omega$, where R_h is the local respiration [mol m^{-2} s^{-1}], V_m is the maximum respiration rate [mol m^{-2} s^{-1}] from the surface of grains, and Ω

is the length of the solid–liquid interface [m]. As expected, $\tilde{R_h}$ increases as the characteristic grain size (λ_c) decreases, due to the increase in the surface area.

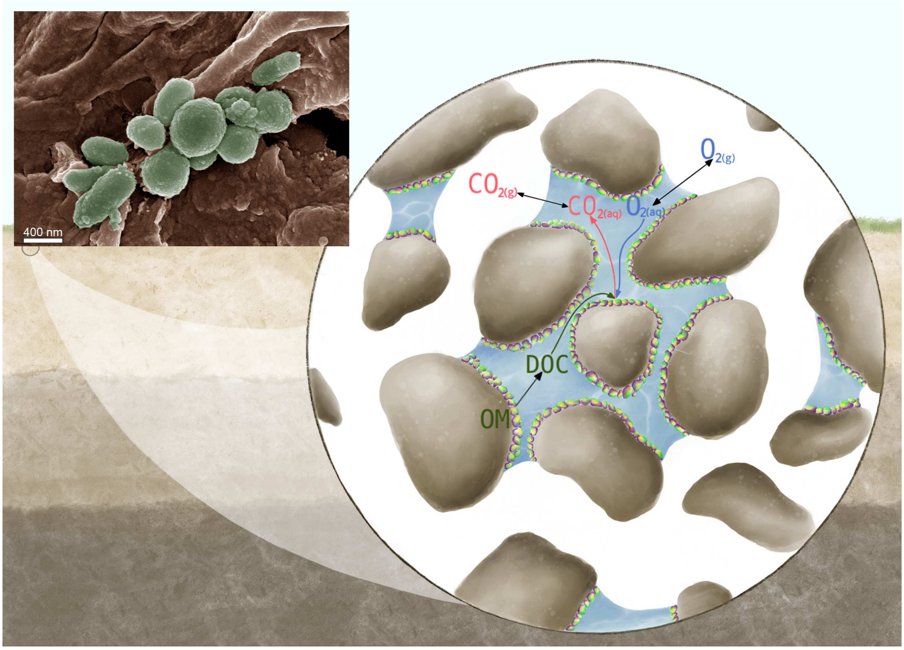

Fig. 1: Schematic of the reactive transport model at the pore-scale. $O_{2(g)}$ diffuses from the atmosphere (gas phase) and is dissolved to the liquid phase ($O_{2(aq)}$) according to Henry's law. Simultaneously, dissolved organic carbon (DOC) is released from soil organic matter (OM). In the presence of both $O_{2(aq)}$ and DOC, aerobic heterotrophic respiration occurs at the interface between the aqueous phase (blue) and the surface of soil grains (brown) by attached microbes (biofilms). As a result, $CO_{2(aq)}$ is released to the water and to the atmosphere $CO_{2(g)}$. In the inset, a scanning electron microscope image shows a cluster of bacteria (greenish colored) around a micrometer root (brown); false coloring was applied for illustration purposes.

To make the connection between pores and continuum (bulk) scale processes, we examine the flux $\tilde{R_h}$ as a function of the number of water patches [21] in the domain N_c and the mean characteristic size of those water patches S_c, both dependent on saturation degree $\tilde{\theta}$. Simulations show that there is a characteristic scaling relation $\tilde{R_h}/N_c \sim S_c^{0.5}$, which indicates a proportionality between the respiration rate within a single water patch and its size (dots in Fig. 2a).

From the scaling laws of percolation theory [18], we derive the characteristic number (N_c) and sizes (S_c) of water patches within the domain [21], for different water saturation degrees (see Methods). The resulting theoretical relations

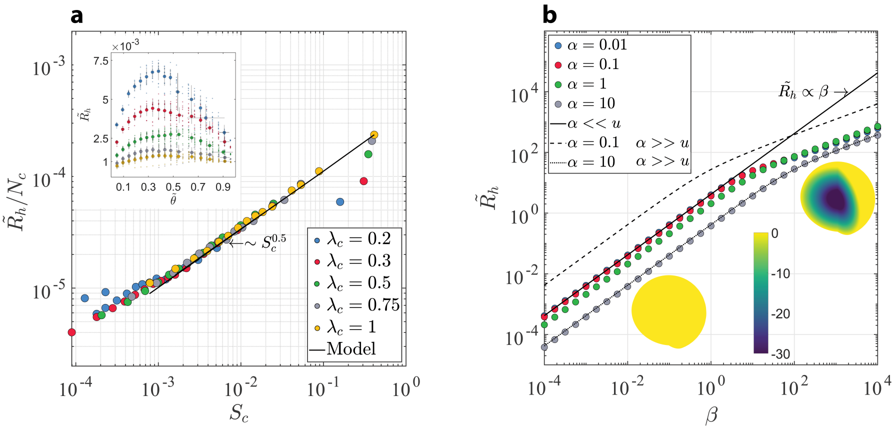

Fig. 2: (**a**) Simulated mean heterotrophic respiration rate per water patch ($\tilde{R}_h/N_c$) as a function of the water patch characteristic size (S_c). The inset shows the non-monotonic relationship between the mean soil HR ($\tilde{R}_h$) and soil saturation ($\tilde{\theta}$), for different grain sizes λ_c. The error bars represent the standard deviation of 20 realizations. **(b)** Dimensionless heterotrophic respiration at the scale of a single water patch as a function of β, for different α values (Methods, Eq. 7). The solid lines represent the analytical solutions (Methods) for the limiting cases; u is the dimensionless substrate concentration. Insets show the spatial distribution of the reaction within a water patch ($\alpha = 0.1$), for $\beta = 0.1$ (left inset) and $\beta = 1000$ (right inset). The colorbar represent the dimensionless respiration rate at logarithmic scale.

of N_c and S_c to $\tilde{\theta}$ at the continuum scale (Eqs. 2, 3 in Methods) were compared successfully against the results from numerical percolation simulations, and are shown in Extended Data Fig. 2a,b. In addition, to further validate Eqs. 2 and 3, we conducted laboratory drainage experiments using microfluidic chips with different grain sizes λ_c, in which we compared simulated and observed water patch properties (Methods and Extended Data Fig. 2c,d).

2.2 Soil heterotrophic respiration at the patch scale

Following the results of pore-scale simulations in Fig. 2a, which demonstrate the basic relation between water patch size (S_c) and respiration rate, we can now generalize the problem to account for variation in environmental conditions (i.e., soil texture, temperature, substrate concentration, diffusion and reaction parameters) by formulating a steady-state Diffusion Reaction Equation (DRE) at the scale of a single water patch. The mathematical formulation is based on three general assumptions: (i) the reactive volume can be treated as homogeneous within the water patch and proportional to the grain surface area, (*ii*) the substrate (dissolved organic carbon) concentration is uniformly distributed within the water patch, and (*iii*) at steady state conditions, microbial activity is proportional to the substrate fluxes.

In non-dimensional form, with symmetrical and spherical coordinates, the DRE can be written as (see Methods for the mathematical development),

$$\frac{d^2u}{d\chi^2} + \frac{2}{\chi}\frac{du}{d\chi} = \frac{\beta u}{u+\alpha}, \tag{1}$$

where u is the normalized oxygen concentration, β and α account for the biophysical parameters of the soil, solute, reaction, and characteristic water patch (Methods Eq. 6), and χ is the normalized spatial coordinate. An analytical solution for Eq. 1 is not available, except for limiting cases ($\alpha << u$ or $\alpha >> u$). We can, however, solve Eq. 1 numerically, to obtain the (non-dimensional) total respiration rate as a function of β for example, for different α values for a characteristic water patch (dots in Fig. 2b). To examine the validity of Eq. 1, we compare it with the results from the 2D numerical reactive transport simulations (Fig. 2a). The solid black line in Fig. 2a represents the numerical solution of Eq. 1 for $\lambda_c = 1$ [mm].

Numerical solution of Eq. 1 reveals the effect of β on HR at water patch scale for different α values (dots in Fig. 2b). High β values are associated with large water patches (i.e., high $\tilde{\theta}$), porous media with high surface area (i.e, small λ_c), small diffusion coefficient (e.g., at low temperature) and high reaction rates. As a consequence, at high β, the local reaction rate within a water patch shows spatial variability, where dissolved O_2 is rapidly consumed at the surface of the patch and does not penetrate into the patch's interior (Fig. 2b right inset, $\beta = 1000$). On the other hand, at low β values, reaction production is uniform in space (Fig. 2b left inset, $\beta = 0.1$), and there is no O_2 limitation within the water patch. In general, as the values of α decrease and β increase, more respiration (i.e., CO_2 efflux) takes place in the water patch; for more details see Methods.

To test our modelling framework, we compared the simulated and observed HR rates with published laboratory and field measurements demonstrating the dependence on soil saturation [22, 23] and temperature [24, 25]. To define the soil parameters for these comparisons, the reported soil texture was used to estimate λ_c [26] and porosity ϕ. Other parameters (e.g., diffusion coefficient, oxygen concentration) were derived using the temperature conditions, while the substrate (DOC) concentration was assumed saturated with respect to Michaelis–Menten kinetics. Despite the considerable experimental scatter and the uncertainties inherent in initializing some of the model parameters, the observations and model outputs were in good agreement (Extended data Fig. 3a,b).

2.3 Soil heterotrophic respiration at global scale

To validate the predictions from our model for various climatic locations, we compare the results with the global soil respiration database [27] (Extended

Data Fig. 3c). To estimate the model parameters (Eqs. 6, 7), we used global databases (at a spatial resolution of 0.25° and at monthly intervals) to characterize the soil temperature and saturation degree [28], soil texture [29], and dissolved organic carbon concentration [30] (for more details see Methods and Extended Data Fig. 5). We computed soil HR at monthly resolution, and aggregated the values to obtain a mean annual HR representing the time period of each observation. Despite large uncertainties in the global climatic and soil databases, the results from our model are in good agreement (RMSE = 0.018).

The globally simulated top soil (0–10 cm depth) annual HR is presented in Fig. 3a. We find that the average global HR rate from the topsoil layer is ~ 282 gC m^{-2} yr^{-1}, which is consistent with previous estimates [5, 31, 32] and represents approximately 70% of current estimates of the total soil HR respiration (about 42 PgC yr^{-1}). This highlights the dominant contribution of the topsoil to soil HR resulting from the fact that this layer is usually under semi-saturated water conditions, at a higher temperature than deeper soil layers, rich in soil organic material, and abundant heterotrophic organisms.

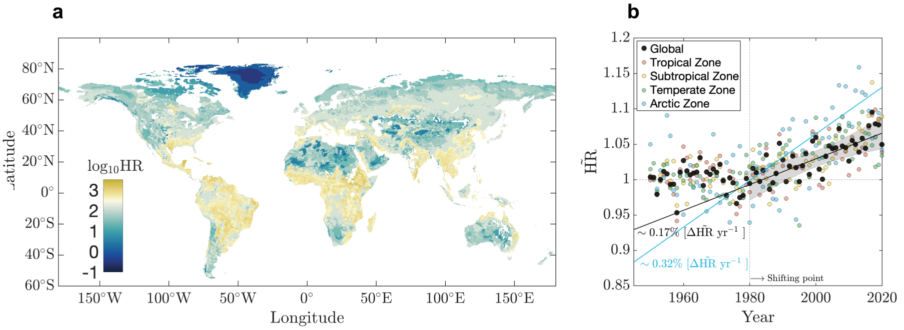

Fig. 3: **(a)** Global map of simulated mean annual soil HR rate (for year 2021); colour bar in logarithmic scale ($\log_{10}$(HR), where HR units are gC m^{-2} yr^{-1}). White regions represent aquatic environments or missing data. **(b)** Temporal trend in soil HR over the period 1948–2021; colours represent different latitudinal climatic regions. The black line is a linear fit to the global data (with shading indicating the 95% confidence interval for the fit), and the cyan line is the fit for the Arctic zone.

2.4 Present and future trends in soil heterotrophic respiration

In light of current trends in surface temperature and soil moisture [1, 33], and the fact that these two are the main factors controlling soil respiration [8], we estimate the temporal evolution of soil HR over the last 73 years (1948–2021) based on these two climatic variables from the Global Land Data Assimilation System database [28] (Fig. 3b). Data for each geographical zone and the global value are normalized by the mean soil HR from 1948 to 1980. A statistically significant trend ($p < 0.01$; Mann–Kendall test) is seen from 1980 onwards, where soil HR shows an average global increase of 0.17% ± 0.05% each year. This is equivalent to an average increase of around 7 gC m^{-2} per decade. Similar trends are found for all geographical zones except the Arctic, where model output suggests a greater increase of 0.32% ± 0.11% annually. These findings are in agreement with field observations for 1989–2008 [27] and with remote sensing data for 2000–2014 [34] of the overall soil respiration.

The global trend estimated by our model is roughly 1.5 times higher than previous estimates computed using a machine learning algorithm [35] (based on the SRDB database [27], with low temporal resolution and for the entire soil column. The topsoil layer is an interface to the atmosphere and thus is more sensitive to environmental feedback and changes. Hence, the discrepancy between the two models, which use different approaches (mechanistic and data-driven) and soil layers, falls within reasonable limits. In the Arctic zone, although the change in HR is already meaningfully higher than in the other geographical regions ($\sim \times 2$), soil HR shows highly scattered values (Fig. 3b). This is due to extreme fluctuations between seasons in the Arctic; as an example, in 2010, due to the extremely hot summer [36], the model indicates a 15% increase in soil HR compared to the baseline. As these fluctuations have become more frequent in the last decade (Fig. 3b, 2010 onwards), soil HR in the Arctic might increase considerably faster than 0.32% per year.

Finally, to predict potential future trends, we used data from 10 Earth System Models (Coupled Model Intercomparison Project phase 6, CMIP6 [37], resolution of 1° and monthly) to assess how changes in surface temperature and soil moisture might affect the evolution of soil HR until the end of the century (Fig. 4a). We employ the worst-case greenhouse gas emission scenario (SSP5-8.5 scenario) as an upper limit for future projections of soil HR. On this basis, the model predicts a dramatic increase in soil HR emission in all geographical zones (~40%), with a much greater increase in the Arctic zone (~ 100% increase by 2100).

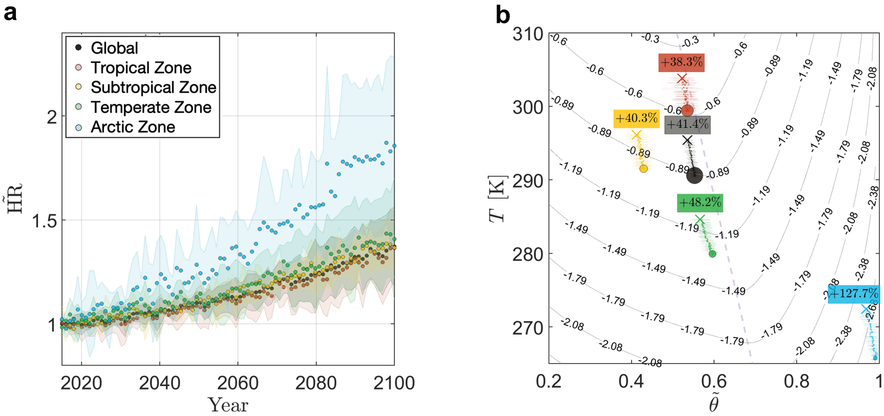

Fig. 4: **(a)** Future projections of soil HR based on our model, for different geographical regions. Points represent HR estimates based on the ensemble average of ten CMIP6 climate models (SSP5-8.5), which were used to initialize the model parameters of surface temperature and soil moisture; climate model uncertainty is represented as minimum and maximum estimates of soil HR among the ensemble (shaded areas). **(b)** Surface map of soil HR ($\log_{10}$ scale) as a function of the soil moisture ($\tilde{\theta}$) and surface temperature (T). The model was parameterized under the average global conditions of soil grain size and substrate concentration. The large point for each geographical zone corresponds to its current state in 2021, with symbol size representing the relative contribution to global soil HR (Tropical 67%, Subtropical 23%, Temperate 10% and Arctic 0.1%). Projected annual changes in soil moisture and surface temperature are indicated by small points; the variance between the climatic models is represented by the error-bars along each trajectory. The symbol × at the end of each trajectory represents the predicted variable values at the end of the century. The dashed purple line indicates the peak of the HR.

To better understand the mechanisms underlying the HR predicted trends, we computed and displayed the projected soil HR as a function of the surface temperature and soil saturation (Fig. 4b). All geographical zones are predicted to experience a strong increase in surface temperature and a moderate decrease in saturation (Fig. 4b); this is predicted to result in a strong increase in the soil HR rate (percentage values within Fig. 4b). The increase of surface temperature and decrease of soil moisture cause the soil HR to increase in parallel with the surface maximal gradient, which leads to a (near) maximal rate-of-change in the tropical and temperate zones — and also globally. Notably, some of the geographical zones are in the vicinity of the maximum HR potential (purple dashed line) based on their mean temperature and soil moisture (most clearly the tropical and temperate zones). This might suggest an adjustment of the soil microbial activity to maximum production in these zones. Changes in soil HR in all geographical zones except the Arctic show an increase of 38–48%

by the end of the century (Fig. 4b). The Arctic zone occupies a unique place on this surface. While current observations reveal a considerable increase in surface temperature but little change in soil moisture, climate models project instead a future decrease in soil moisture, which results in a sharp increase in the predicted soil HR by $> 100\%$. This strong increase stems from the curvature of the HR surface at the Arctic location, where the maximum change is oriented upwards and to the left on the surface. The model response surface indicates that a reduction in soil moisture, in all zones except in the Arctic, will lead to a reduction in soil HR.

3 Discussion

We have presented a biophysical model to estimate soil heterotrophic respiration from climatic data. The principal innovation of our approach is the mechanistic perspective on soil HR from pore to global scales, in the absence of any empirical parameters, which enables robust quantification of current HR rates and future trends. The simplicity of the model is encapsulated by the two variables, α and β (Methods Eq. 6), that control the respiration rate at the scale of a single water patch (Fig. 2b). Moreover, as the value of α is strictly limited ($0.01 < \alpha < 0.5$) for aerobic respiration, it is mainly β that controls the reaction rate within a single patch (Extended Data Fig. 4b). We validated the model against controlled laboratory measurements, and against field observations, and find a good agreement with the predictions (Extended Data Fig. 3).

A fundamental assumption of the model is that the ambient conditions control microbial functioning [38], despite the taxonomic diversity of microbes on Earth [39, 40]. This assumption is supported by the relative importance of β over α (Fig. 2b) in determining HR rate at the single patch level, as β characterizes the environmental conditions while α accounts for microbial activity.

As demonstrated by the global-scale analysis (Fig. 3b), HR from the topsoil layer is increasing globally at a rate of about 1.7% per decade (equivalent to an increase of about 0.9 PgC per decade). This trend is similar in all geographical locations, except for the Arctic zone, where the rate is almost double the global mean (3.2% per decade). Based on projections of changes in soil temperature and moisture obtained from climate models, we demonstrated that future trends indicate a gradual increase in annual soil HR rate until the end of the century (5% per decade), with a greater increase (14% per decade) in the Arctic zone (Fig. 4a). Within the Arctic zone, unlike other climatic zones, the change in soil HR is principally driven by a projected reduction in soil moisture rather than by the increase in temperature (Fig. 4b). According to current observations, the soil moisture content in the Arctic does not yet show a negative trend and remains on average close to saturation. The increase in soil respiration in the Arctic over the last four decades (Fig. 3b) is thus still mainly due to increasing surface temperature, and the onset of declining soil moisture may represent a tipping point.

Our model does not take into account temporal changes in dissolved organic carbon concentrations in the soil, as supported by observations [41],; in contrast, we consider the temporal changes in soil water content and temperature as an indicator of the availability of dissolved organic carbon for heterotrophic respiration. The modelled temporal trends of soil HR, which are consistent with observations [5, 31, 32], imply that surface temperature and soil moisture are the main controls of the HR rate and, thus, the availability of dissolved organic carbon. At large time scales, carbon efflux cannot exceed the carbon influx by Gross Primary Production. The ratio between HR and autotrophic respiration has increased over the past three decades [9]. Those two facts, together with the predicted HR increase, are a manifestation of the non-equilibrium conditions of the terrestrial ecosystem, where HR, at short time scales (i.e., up to hundreds of years), is independent of Gross Primary Production, eventually leading to a loss of the soil carbon stocks [42, 43]. How future changes in the Earth's climatic environment will affect the terrestrial carbon cycle is one of the primary concerns of the 21st century, and this study sheds light on one of its primary mechanisms.

References

[1] IPCC: Climate Change 2021: The Physical Science Basis. Contribution of Working Group I to the Sixth Assessment Report of the Intergovernmental Panel on Climate Change. Cambridge University Press. In Press. (2021)

[2] Raich, J.W., Schlesinger, W.H.: The global carbon dioxide flux in soil respiration and its relationship to vegetation and climate. Tellus B: Chemical and Physical Meteorology **44**(2), 81–99 (1992) https://doi.org/10.3402/tellusb.v44i2.15428. https://doi.org/10.3402/tellusb.v44i2.15428

[3] Li, W., Ciais, P., Wang, Y., Peng, S., Broquet, G., Ballantyne, A.P., Canadell, J.G., Cooper, L., Friedlingstein, P., Le Quéré, C., Myneni, R.B., Peters, G.P., Piao, S., Pongratz, J.: Reducing uncertainties in decadal variability of the global carbon budget with multiple datasets. Proceedings of the National Academy of Sciences **113**(46), 13104–13108 (2016). https://doi.org/10.1073/pnas.1603956113

[4] Tharammal, T., Bala, G., Devaraju, N., Nemani, R.: A review of the major drivers of the terrestrial carbon uptake: model-based assessments, consensus, and uncertainties. Environmental Research Letters **14**(9), 093005 (2019). https://doi.org/10.1088/1748-9326/AB3012

[5] Konings, A.G., Bloom, A.A., Liu, J., Parazoo, N.C., Schimel, D.S.,

Bowman, K.W.: Global satellite-driven estimates of heterotrophic respiration. Biogeosciences **16**(11), 2269–2284 (2019). https://doi.org/10.5194/bg-16-2269-2019

[6] Pries, C.E.H., Castanha, C., Porras, R.C., Torn, M.S.: The whole-soil carbon flux in response to warming. Science **355**(6332), 1420–1423 (2017) https://www.science.org/doi/pdf/10.1126/science.aal1319. https://doi.org/10.1126/science.aal1319

[7] Totsche, K.U., Rennert, T., Gerzabek, M.H., Kögel-Knabner, I., Smalla, K., Spiteller, M., Vogel, H.-J.: Biogeochemical interfaces in soil: The interdisciplinary challenge for soil science. Journal of Plant Nutrition and Soil Science **173**(1), 88–99 (2010). https://doi.org/10.1002/jpln.200900105

[8] Davidson, E.A., Janssens, I.A.: Temperature sensitivity of soil carbon decomposition and feedbacks to climate change. Nature **440**(7081), 165–173 (2006). https://doi.org/10.1038/nature04514

[9] Bond-Lamberty, B., Bailey, V.L., Chen, M., Gough, C.M., Vargas, R.: Globally rising soil heterotrophic respiration over recent decades. Nature **560**(7716), 80–83 (2018). https://doi.org/10.1038/s41586-018-0358-x

[10] Lloyd, J., Taylor, J.A.: On the temperature dependence of soil respiration. Functional Ecology **8**(3), 315–323 (1994). https://doi.org/10.2307/2389824. Full publication date: Jun., 1994

[11] Dacal, M., Delgado-Baquerizo, M., Barquero, J., Berhe, A.A., Gallardo, A., Maestre, F.T., García-Palacios, P.: Temperature increases soil respiration across ecosystem types and soil development, but soil properties determine the magnitude of this effect. Ecosystems (2021). https://doi.org/10.1007/s10021-021-00648-2

[12] Skopp, J., Jawson, M.D., Doran, J.W.: Steady-state aerobic microbial activity as a function of soil water content. Soil Science Society of America Journal **54**(6), 1619–1625 (1990). https://doi.org/10.2136/sssaj1990.03615995005400060018x

[13] Moyano, F.E., Manzoni, S., Chenu, C.: Responses of soil heterotrophic respiration to moisture availability: An exploration of processes and models. Soil Biology and Biochemistry **59**, 72–85 (2013). https://doi.org/10.1016/j.soilbio.2013.01.002

[14] Yan, Z., Liu, C., Todd-Brown, K.E., Liu, Y., Bond-Lamberty, B., Bailey, V.L.: Pore-scale investigation on the response of heterotrophic respiration to moisture conditions in heterogeneous soils. Biogeochemistry **131**(1), 121–134 (2016). https://doi.org/10.1007/s10533-016-0270-0

[15] Yan, Z., Bond-Lamberty, B., Todd-Brown, K.E., Bailey, V.L., Li, S., Liu, C., Liu, C.: A moisture function of soil heterotrophic respiration that incorporates microscale processes. Nature Communications **9**(1), 2562 (2018). https://doi.org/10.1038/s41467-018-04971-6

[16] Davidson, E.A., Verchot, L.V., Cattânio, J.H., Ackerman, I.L., Carvalho, J.E.M.: Effects of soil water content on soil respiration in forests and cattle pastures of eastern amazonia. Biogeochemistry **48**(1), 53–69 (2000). https://doi.org/10.1023/A:1006204113917

[17] Hashimoto, S., Carvalhais, N., Ito, A., Migliavacca, M., Nishina, K., Reichstein, M.: Global spatiotemporal distribution of soil respiration modeled using a global database. Biogeosciences **12**(13), 4121–4132 (2015). https://doi.org/10.5194/bg-12-4121-2015

[18] Stauffer, D.: Scaling theory of percolation clusters. Physics Reports **54**(1), 1–74 (1979). https://doi.org/10.1016/0370-1573(79)90060-7

[19] Gostick, J.T., Misaghian, N., Yang, J., Boek, E.S.: Simulating volume-controlled invasion of a non-wetting fluid in volumetric images using basic image processing tools. Computers and Geosciences **158**, 104978 (2022). https://doi.org/10.1016/j.cageo.2021.104978

[20] Inc., C.: COMSOL (2020). http://www.comsol.com/products/multiphysics/

[21] Bickel, S., Or, D.: Soil bacterial diversity mediated by microscale aqueous-phase processes across biomes. Nature Communications **11**(1), 116 (2020). https://doi.org/10.1038/s41467-019-13966-w

[22] Franzluebbers, A.J.: Microbial activity in response to water-filled pore space of variably eroded southern piedmont soils. Applied Soil Ecology **11**, 91–101 (1999)

[23] Zheng, P., Wang, D., Yu, X., Jia, G., Liu, Z., Wang, Y., Zhang, Y.: Effects of drought and rainfall events on soil autotrophic respiration and heterotrophic respiration. Agriculture, Ecosystems and Environment **308**, 107267 (2021). https://doi.org/10.1016/j.agee.2020.107267

[24] Yan, D., Li, J., Pei, J., Cui, J., Nie, M., Fang, C.: The temperature sensitivity of soil organic carbon decomposition is greater in subsoil than in topsoil during laboratory incubation. Scientific Reports **7**(1), 5181 (2017). https://doi.org/10.1038/s41598-017-05293-1

[25] Lu, H., Liu, S., Wang, H., Luan, J., Schindlbacher, A., Liu, Y., Wang, Y.: Experimental throughfall reduction barely affects soil carbon dynamics in a warm-temperate oak forest, central china. Scientific Reports **7**(1), 15099

(2017). https://doi.org/10.1038/s41598-017-15157-3

[26] Shirazi, M.A., Boersma, L.: A unifying quantitative analysis of soil texture. Soil Science Society of America Journal **48**(1), 142–147 (1984). https://doi.org/10.2136/sssaj1984.03615995004800010026x

[27] Jian, J., Vargas, R., Anderson-Teixeira, K., Stell, E., Herrmann, V., Horn, M., Kholod, N., Manzon, J., Marchesi, R., Paredes, D., Bond-Lamberty, B.: A restructured and updated global soil respiration database (srdb-v5). Earth System Science Data **13**(2), 255–267 (2021). https://doi.org/10.5194/essd-13-255-2021

[28] Rodell, M., Houser, P.R., Jambor, U., Gottschalck, J., Mitchell, K., Meng, C.-J., Arsenault, K., Cosgrove, B., Radakovich, J., Bosilovich, M., Entin, J.K., Walker, J.P., Lohmann, D., Toll, D.: The global land data assimilation system. Bulletin of the American Meteorological Society **85**(3), 381–394 (2004). https://doi.org/10.1175/BAMS-85-3-381

[29] Wieder, W.: Regridded Harmonized World Soil Database v1.2. ORNL Distributed Active Archive Center (2014). https://doi.org/10.3334/ORNLDAAC/1247. http://daac.ornl.gov/cgi-bin/dsviewer.pl?ds_id=1247

[30] Langeveld, J., Bouwman, A.F., van Hoek, W.J., Vilmin, L., Beusen, A.H.W., Mogollón, J.M., Middelburg, J.J.: Estimating dissolved carbon concentrations in global soils: a global database and model. SN Applied Sciences **2**(10), 1626 (2020). https://doi.org/10.1007/s42452-020-03290-0

[31] Warner, D.L., Bond-Lamberty, B.P., Jian, J., Stell, E., Vargas, R.: Global Gridded 1-km Annual Soil Respiration and Uncertainty Derived from SRDB V3. ORNL Distributed Active Archive Center (2019). https://doi.org/10.3334/ORNLDAAC/1736. https://daac.ornl.gov/cgi-bin/dsviewer.pl?ds_id=1736

[32] Ciais, P., Yao, Y., Gasser, T., Baccini, A., Wang, Y., Lauerwald, R., Peng, S., Bastos, A., Li, W., Raymond, P.A., Canadell, J.G., Peters, G.P., Andres, R.J., Chang, J., Yue, C., Dolman, A.J., Haverd, V., Hartmann, J., Laruelle, G., Konings, A.G., King, A.W., Liu, Y., Luyssaert, S., Maignan, F., Patra, P.K., Peregon, A., Regnier, P., Pongratz, J., Poulter, B., Shvidenko, A., Valentini, R., Wang, R., Broquet, G., Yin, Y., Zscheischler, J., Guenet, B., Goll, D.S., Ballantyne, A.-P., Yang, H., Qiu, C., Zhu, D.: Empirical estimates of regional carbon budgets imply reduced global soil heterotrophic respiration. National Science Review **8**(2) (2020). https://doi.org/10.1093/nsr/nwaa145

[33] Deng, Y., Wang, S., Bai, X., Luo, G., Wu, L., Cao, Y., Li, H., Li, C., Yang, Y., Hu, Z., Tian, S.: Variation trend of global soil moisture and its cause analysis. Ecological Indicators **110**, 105939 (2020). https://doi.org/

10.1016/j.ecolind.2019.105939

[34] Huang, N., Wang, L., Song, X.-P., Black, T.A., Jassal, R.S., Myneni, R.B., Wu, C., Wang, L., Song, W., Ji, D., Yu, S., Niu, Z.: Spatial and temporal variations in global soil respiration and their relationships with climate and land cover. Science Advances **6**(41), 8508 (2020). https://doi.org/10.1126/sciadv.abb8508

[35] Tang, X., Fan, S., Du, M., Zhang, W., Gao, S., Liu, S., Chen, G., Yu, Z., Yang, W.: Spatial and temporal patterns of global soil heterotrophic respiration in terrestrial ecosystems. Earth System Science Data **12**(2), 1037–1051 (2020). https://doi.org/10.5194/essd-12-1037-2020

[36] Barriopedro, D., Fischer, E.M., Luterbacher, J., Trigo, R.M., García-Herrera, R.: The hot summer of 2010: Redrawing the temperature record map of europe. Science **332**(6026), 220–224 (2011). https://doi.org/10.1126/science.1201224

[37] Eyring, V., Bony, S., Meehl, G.A., Senior, C.A., Stevens, B., Stouffer, R.J., Taylor, K.E.: Overview of the coupled model intercomparison project phase 6 (cmip6) experimental design and organization. Geoscientific Model Development **9**(5), 1937–1958 (2016). https://doi.org/10.5194/gmd-9-1937-2016

[38] Dacal, M., Bradford, M.A., Plaza, C., Maestre, F.T., García-Palacios, P.: Soil microbial respiration adapts to ambient temperature in global drylands. Nature Ecology & Evolution **3**(2), 232–238 (2019). https://doi.org/10.1038/s41559-018-0770-5

[39] Guerra, C.A., Heintz-Buschart, A., Sikorski, J., Chatzinotas, A., Guerrero-Ramírez, N., Cesarz, S., Beaumelle, L., Rillig, M.C., Maestre, F.T., Delgado-Baquerizo, M., Buscot, F., Overmann, J., Patoine, G., Phillips, H.R.P., Winter, M., Wubet, T., Küsel, K., Bardgett, R.D., Cameron, E.K., Cowan, D., Grebenc, T., Marín, C., Orgiazzi, A., Singh, B.K., Wall, D.H., Eisenhauer, N.: Blind spots in global soil biodiversity and ecosystem function research. Nature Communications **11**(1), 3870 (2020). https://doi.org/10.1038/s41467-020-17688-2

[40] Bastida, F., Eldridge, D.J., García, C., Kenny Png, G., Bardgett, R.D., Delgado-Baquerizo, M.: Soil microbial diversity–biomass relationships are driven by soil carbon content across global biomes. The ISME Journal **15**(7), 2081–2091 (2021). https://doi.org/10.1038/s41396-021-00906-0

[41] Gubler, A., Wächter, D., Schwab, P., Müller, M., Keller, A.: Twenty-five years of observations of soil organic carbon in swiss croplands showing stability overall but with some divergent trends. Environmental Monitoring and Assessment **191**(5), 277 (2019). https://doi.org/10.1007/

s10661-019-7435-y

[42] Knorr, W., Prentice, I.C., House, J.I., Holland, E.A.: Long-term sensitivity of soil carbon turnover to warming. Nature **433**(7023), 298–301 (2005). https://doi.org/10.1038/nature03226

[43] Duffy, K.A., Schwalm, C.R., Arcus, V.L., Koch, G.W., Liang, L.L., Schipper, L.A.: How close are we to the temperature tipping point of the terrestrial biosphere? Science Advances **7**(3), 1052 (2021). https://doi.org/10.1126/sciadv.aay1052

[44] Gostick, J.T., Khan, Z.A., Tranter, T.G., Kok, M.D.r., Agnaou, M., Sadeghi, M., Jervis, R.: Porespy: A python toolkit for quantitative analysis of porous media images. Journal of Open Source Software **4**(37), 1296 (2019). https://doi.org/10.21105/joss.01296

[45] Anbari, A., Chien, H.-T., Datta, S.S., Deng, W., Weitz, D.A., Fan, J.: Microfluidic model porous media: Fabrication and applications. Small **14**(18), 1703575 (2018). https://doi.org/10.1002/smll.201703575

[46] Davidson, E.A., Samanta, S., Caramori, S.S., Savage, K.: The dual arrhenius and Michaelis–Menten kinetics model for decomposition of soil organic matter at hourly to seasonal time scales. Global Change Biology **18**(1), 371–384 (2012). https://doi.org/10.1111/j.1365-2486.2011.02546.x

[47] Linstrom, P.: NIST Chemistry WebBook, NIST Standard Reference Database 69. National Institute of Standards and Technology. Type: dataset (1997). https://doi.org/10.18434/T4D303. http://webbook.nist.gov/chemistry/ Accessed 2022-02-21

[48] German, D.P., Marcelo, K.R.B., Stone, M.M., Allison, S.D.: The Michaelis–Menten kinetics of soil extracellular enzymes in response to temperature: a cross-latitudinal study. Global Change Biology **18**(4), 1468–1479 (2012). https://doi.org/10.1111/j.1365-2486.2011.02615.x

[49] Eberwein, J., Shen, W., Jenerette, G.D.: Michaelis-Menten kinetics of soil respiration feedbacks to nitrogen deposition and climate change in subtropical forests. Scientific Reports **7**(1), 1752 (2017). https://doi.org/10.1038/s41598-017-01941-8

[50] Han, P., Bartels, D.M.: Temperature dependence of oxygen diffusion in H_2O and D_2O. The Journal of Physical Chemistry **100**(13), 5597–5602 (1996) https://doi.org/10.1021/jp952903y. https://doi.org/10.1021/jp952903y

[51] Borkovec, M., Wu, Q., Sticher, H., Degovics, G., Laggner, P.: Surface area and size distributions of soil particles. In: Tadros, T.F.,

Gregory, J. (eds.) Colloids in the Aquatic Environment, pp. 65–76. Elsevier, Oxford (1993). https://doi.org/10.1016/B978-1-85861-038-2.50008-5. https://www.sciencedirect.com/science/article/pii/B9781858610382500085

[52] Fatichi, S., Ivanov, V.Y., Paschalis, A., Peleg, N., Molnar, P., Rimkus, S., Kim, J., Burlando, P., Caporali, E.: Uncertainty partition challenges the predictability of vital details of climate change. Earth's Future **4**(5), 240–251 (2016). https://doi.org/10.1002/2015EF000336

[53] Knutti, R., Masson, D., Gettelman, A.: Climate model genealogy: Generation cmip5 and how we got there. Geophysical Research Letters **40**(6), 1194–1199 (2013). https://doi.org/10.1002/grl.50256

[54] O'Neill, B.C., Tebaldi, C., van Vuuren, D.P., Eyring, V., Friedlingstein, P., Hurtt, G., Knutti, R., Kriegler, E., Lamarque, J.-F., Lowe, J., Meehl, G.A., Moss, R., Riahi, K., Sanderson, B.M.: The scenario model intercomparison project (scenariomip) for CMIP6. Geoscientific Model Development **9**(9), 3461–3482 (2016). https://doi.org/10.5194/gmd-9-3461-2016

[55] Franzluebbers, A.J.: Microbial activity in response to water-filled pore space of variably eroded southern piedmont soils. Applied Soil Ecology **11**(1), 91–101 (1999). https://doi.org/10.1016/S0929-1393(98)00128-0

[56] Zhang, Y., Schaap, M.G.: Weighted recalibration of the rosetta pedotransfer model with improved estimates of hydraulic parameter distributions and summary statistics (rosetta3). Journal of Hydrology **547**, 39–53 (2017). https://doi.org/10.1016/j.jhydrol.2017.01.004

[57] Hou, C., Gheorghiu, S., Huxley, V.H., Pfeifer, P.: Reverse engineering of oxygen transport in the lung: Adaptation to changing demands and resources through space-filling networks. PLOS Computational Biology **6**(8), 1–12 (2010). https://doi.org/10.1371/journal.pcbi.1000902

[58] Balch, J., Guéguen, C.: Effects of molecular weight on the diffusion coefficient of aquatic dissolved organic matter and humic substances. Chemosphere **119**, 498–503 (2015). https://doi.org/10.1016/j.chemosphere.2014.07.013

[59] Magliaro, C., Mattei, G., Iacoangeli, F., Corti, A., Piemonte, V., Ahluwalia, A.: Oxygen consumption characteristics in 3D constructs depend on cell density. Frontiers in Bioengineering and Biotechnology **7** (2019). https://doi.org/10.3389/fbioe.2019.00251

4 Methods

4.1 Image-based invasion percolation algorithm

An image-based invasion percolation algorithm [19, 44] was used to simulate the water spatial distribution at different saturation degrees ($\tilde{\theta}$) for different porous medium configurations. The porous materials were generated using randomly distributed grains of a uniform diameter (λ_c) within the domain (20 realizations for each λ_c); each porous medium system had overall dimensions of 3 cm (width) × 2.25 cm (height), and a porosity of 0.5. Initially, the domain is filled with water, and during the invasion percolation process, the air is entering from the upper boundary of the system and invades the liquid phase, following the capillary entry conditions at the air–water interface. At the end of the simulations, the percolation clusters (Extended Data Fig. 1a) and thus the distribution of water patches within the domain (Extended Data Fig. 1b) is obtained at different saturation degrees. Note that even though we used a uniform grain size for each realization, the resulting simulated porous media are highly heterogeneous in their pore size distributions (see inset in Extended Data Fig. 1b as an example). For more details see [44].

4.1.1 Estimating water patch proportionalities from percolation theory

From percolation theory, we expect that the size distribution of water patches $n(s)$ in the domain follows a general proportionality [18], $n(s) = s^{-\tau}\exp(-s/\xi)$, where s is the water patch size, τ is the Fisher exponent, which depends on the dimensionality of the system, and ξ is a cut-off parameter, which depends on the porous medium properties and the saturation degree [21]. From this definition of $n(s)$, we calculate the characteristic number of patches in the domain using the mean of the distribution function, $N_c = \int_0^1 n(\tilde{s})d\tilde{s}$ (where $\tilde{s} = s/\theta_s$), which yields $N_c = \left(\frac{1}{\xi}\right)^{\tau-1}\Gamma(1-\tau) - E_\tau\left(\frac{1}{\xi}\right)$, where Γ is the gamma function and E_τ is the exponential integral function. From mass conservation, the characteristic patch size is

$$S_c = \tilde{\theta}/N_c. \tag{2}$$

From percolation simulations, the value of ξ is found to depend on $\tilde{\theta}$ as $\xi = \gamma(1-\tilde{\theta})$, with $\gamma = 100$. Finally, to account for the total number of water patches in the domain of length scale L, N_c is normalized by $N^0 = \left(\frac{L}{\lambda_c}\right)^{d(1-\tilde{\theta})}$ [21], to yield

$$N_c(\tilde{\theta},\lambda_c) \approx N^0(\tilde{\theta},\lambda_c)\left(\frac{1}{\xi(\tilde{\theta})}\right)^{\tau-1}\Gamma(1-\tau) - E_\tau\left(\frac{1}{\xi(\tilde{\theta})}\right), \tag{3}$$

where d is the dimensionality ($d = 2$ for the numerical simulations). According to this formulation, under fully saturated conditions ($\tilde{\theta} = 1$), $N_c = 1$ (thus a single water cluster) and the characteristic patch S_c has the size of the entire system voids. The resulting theoretical relations of N_c and S_c to $\tilde{\theta}$ at the continuum scale (Eqs. 2–3) are shown in Extended Data Fig. 2a and b, respectively, and compared to the numerical percolation simulations.

4.2 Microfluidic experiments

To support the relationships between water patch properties and soil saturation degree (Eqs. 2,3) obtained from percolation theory, we performed microfluidic experiments. Microfluidic chips were fabricated using soft lithography [45]. Each chip had overall dimensions 5 cm × 5 cm × 0.005 cm. Similar to the numerical simulations (Methods), the solid phase was generated by randomly distributing circular objects (”grains”) with diameter λ_c mm. To mimic the invasion percolation algorithm, the microfluidic chips were placed with a long axis vertical and saturated with water (dyed with fluorescein solution of 0.01 mM) as initial condition. The upper side of each chip was open to the atmosphere, and the lower side was open for drainage. The air and water phases were monitored during the drainage process using a CCD camera (Ximea, Germany), and the relationship between the number and size of water patches and the saturation degree was obtained by image analysis (Extended Data Fig. 2).

The divergence of the experimental data (Extended Data Fig. 2) from theory observed at very low saturation conditions is expected (as $\tilde{\theta} \to 0$, also $N_c \to 0$), because the relations in Eqs. 2–3 are derived at the percolation threshold [18] and therefore cannot account for the limiting cases of very high and very low saturation conditions. However, for the range of expected soil saturation levels in natural soils, the theoretical relations fit the laboratory data very well.

4.3 Numerical simulations of the two-phase reaction–diffusion equation in porous media

Based on the water–air spatial distribution from the invasion–percolation simulations, finite-element simulations of the diffusion–reaction equation were performed [20].

Within the system, two phases are considered, the (air) invading phase, Φ_a and the (water) depending phase, Φ_w. Chemical components (i.e., O_2, CO_2 and dissolved organic carbon, C_s) are transported solely by diffusion, where each component has a phase-dependent diffusion coefficient. Surface reactions (Michaelis–Menten kinetics) take place on the perimeter of solid grains [46] in Φ_w, with rate

$$R_{surf} = V_m \frac{C_s}{C_s + K_{m(s)}} \frac{C_{O_2}}{C_{O_2} + K_{m(O_2)}}, \tag{4}$$

where V_m is the maximum local rate of HR reaction [mol s^{-1}m^{-2}], C_{O_2} is the dissolved oxygen concentration, C_s is the substrate concentration and $K_{m(s)}$ and $K_{m(O_2)}$ are the Michaelis constants of the substrate and oxygen, respectively. At the interface of the two phases, mass transfer of chemicals is simulated by Henry's Law [47]. A fixed atmospheric concentration ($C0_{O_2}$) was set as the upper boundary condition for oxygen, while the other external boundaries were treated as open for all species. At the perimeter of the solid grains in Φ_w phase, a constant dissolved organic carbon concentration ($C0_{DOC}$) was set, to describe the organic matter (OM) degradation to dissolved organic carbon (C_s). Then, C_s is transported by diffusion and reacts with dissolved oxygen, C_{O_2} species, to produce dissolved CO_2 (Eq. 4). 20 realizations were performed for each value of λ_c. The parameters used in the numerical simulations are given in Extended Data Table 1.

4.4 Reaction–diffusion equation at the continuum scale for a single water patch

For a single water patch, the dissolved oxygen concentration (C_{O_2}) can be derived by solving the steady-state diffusion–reaction equation (DRE). Assuming that water patches can be approximated by a spherical shape, the DRE can be written as

$$D_m \left(\frac{d^2 C_{O_2}}{dr^2} + \frac{2}{r} \frac{dC_{O_2}}{dr} \right) = \frac{3\phi V_m}{\lambda_c} \frac{C_s}{C_s + K_{m(s)}} \frac{C_{O_2}}{C_{O_2} + K_{m(O_2)}}, \tag{5}$$

where D_m [$\mathrm{m^2\ s^{-1}}$] is the molecular diffusion coefficient of dissolved oxygen in water, ϕ is the medium porosity and r is the radial distance. The term $\frac{3\phi}{\lambda_c}$ is the specific surface area [$\mathrm{m^2\ m^{-3}}$], obtained by assuming spherical grains as the soil particles. By defining the following dimensionless parameters,

$$u = \frac{C_{O_2}}{C_0} \quad ; \ \chi = \frac{r}{r_0} \quad ; \ \alpha = \frac{K_{m(O_2)}}{C_0} \quad ; \ \beta = \frac{3 V_m \phi C_s r_0^2}{D_m \lambda_c C_0 (C_s + K_{m(s)})}, \tag{6}$$

we can rewrite Eq. 5 as

$$\frac{d^2 u}{d\chi^2} + \frac{2}{\chi} \frac{du}{d\chi} = \frac{\beta u}{u + \alpha}. \tag{7}$$

Implementing boundary conditions $u(1) = 1$ and $u'(0) = 0$, Eq. 5 can be solved analytically for the limiting cases

$$u(\chi) = \begin{cases} \frac{1}{6}\beta\left(\chi^2 - 1\right) + 1; & \text{if } \alpha << u \\ \frac{e^{-\frac{\sqrt{\beta}(\chi-1)}{\sqrt{\alpha}}}\left(e^{\frac{2\sqrt{\beta}\chi}{\sqrt{\alpha}}} - 1\right)}{\chi\left(e^{\frac{2\sqrt{\beta}}{\sqrt{\alpha}}} - 1\right)}; & \text{if } \alpha >> u. \end{cases}$$

Otherwise, Eq. 7 can be solved numerically. To derive the characteristic reaction term, i.e., the right-hand side in Eq. 7, the solution for the normalized concentration, $u(\chi)$, is implemented in the reaction term. Then, the reaction rate depending on the radial coordinate can be obtained. Note, in the case of $\alpha << u$, the reaction term is equal to β solely, without any radial dependency.

The analytical solutions for the limiting cases (where $\alpha << u$ or $\alpha >> u$) can be used to delineate the boundaries of the real solutions. As can be seen in Fig. 2b, at low β values, the solutions can be restricted to a relatively narrow range ($\sim$ an order of magnitude) between the two analytical solutions (solid and dashed lines in Fig. 2b). This range increases as β increases. Up to $\beta \approx 10$, the analytical and the full solution (solved numerically) show an excellent match. This suggests that analytical solutions for HR can be useful if β is relatively small ($\beta < 10$). However, the value of β is likely to vary strongly given the variation in the two main components that control soil HR: temperature and soil moisture (Extended Data Fig. 4a). Moreover, as we demonstrate in Fig. 2b, the assumption $\alpha >> u$ leads to a large difference with respect to the real solution when α is relatively small (the upper dashed line shows the analytical solution for $\alpha = 0.1$ [48, 49]). In contrast, for large α (the lower dashed line shows the analytical solution for $\alpha = 10$), the analytical solution captures the numerical solution. However, such higher α values have no meaning for aerobic respiration, where Michaelis constant, K_m, is always smaller than the saturated substrate concentration (i.e. it can be safely assumed that for aerobic microbes, the apparent K_m for respiration is smaller than the maximum O_2 concentration observed at the soil-air interface).

4.5 Global databases and climate projections

To initialize the model parameters, we used a set of global gridded databases at a resolution of 0.25° and monthly time interval. Data came from remote sensing measurements (surface temperature, soil moisture, surface altitude and texture [28]), and by observation interpolation (dissolved organic carbon [30]).

Based on these data sets, for each grid point we derived the following variables:

- Surface temperature
- Atmospheric oxygen concentration, based on the location's altitude and temperature [47]
- Dissolved oxygen concentration (C_0), according to Henry's law [47]
- Oxygen diffusion coefficient in water (D_{O_2}), based on the ambient temperature [50]
- Soil representative grain size (λ_c) [26]
- Soil surface area (SSA) [51]
- Soil saturation degree, and thus the resulting water patch characteristic size (S_c), and the number of patches (N_c).
- Maximum reaction rate, V_m, for Michaelis–Menten kinetics, based on the ambient temperature [46, 48] and the soil surface area
- Dissolved organic carbon concentration [30]

Using these variables, Eqs. 1 - 3 were parameterized to each location on the global grid. In Extended Data Fig. 5, we present a schematic illustration of the model methodology for deriving heterotrophic respiration.

To predict future soil HR, we used climate projections from ten global circulation models from the Coupled Model Intercomparison Project Phase 6 [37]. To maximize climate projection variability [52], we chose climate models that minimized the genealogy similarity between them [53]. We used the following models: ACCESS-CM2, EC-Earth3-Veg-LR, CNRM-CM6-1, NorESM2-MM, MPI-ESM1-2-LR, MIROC6, CanESM5, MIROC6, CMCC-CM2-SR5, CAMS-CSM1-0, and CESM2, and derived two variables: surface temperature and soil moisture in the upper portion of the soil column. The data were obtained with a monthly and 1° resolution from the worst-case greenhouse gas emission scenario (SSP5-8.5 [54]) covering the period between 2015 (used as a reference year to represent present climate conditions) and 2100. Our model was then used to compute soil HR for each grid cell for the entire period. We present results of the simulation summarized for four climate zones: Tropical (0° to 23.5° N/S), Subtropical (23.5° to 40° N/S), Temperate (40° to 65° N/S), and Arctic (65° to 90° N/S). The evolution of soil HR for each of the climate models are presented in Extended Data Fig. 6.

Data availability

The raw data, datasets and computer codes to support all the results and analysis of this study have been deposited in the GitHub repository GitHub repository.

Acknowledgements

We thank Dr. Russell Naisbit for help with editing, and Maya Steindel for the illustration (Fig. 1). A.N. is supported by the ETH Postdoc Fellowship.

Author contributions

A.N., M.H., N.P. and P.M. design the research. A.N., U.A. and N.G. designed and conducted experiments. A.N. developed and preformed the numerical/theoretical simulations. A.N., U.A., N.P., N.G., J.J.M., P.M. and M.H. wrote the manuscript.

5 Extended Data

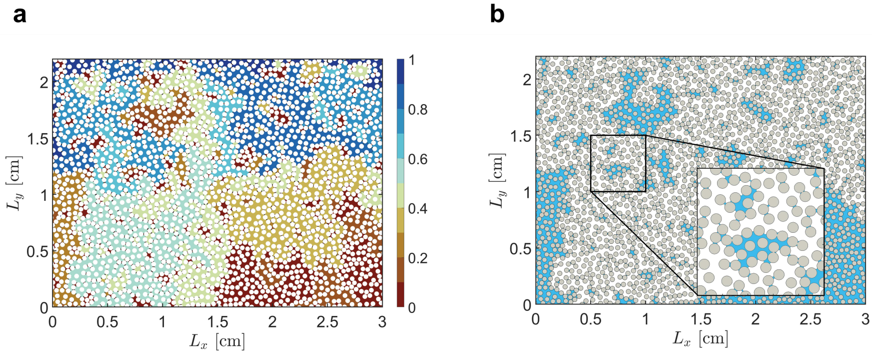

Extended Data Fig. 1: **(a)** Example of a single realization of the invasion–percolation algorithm (λ_c = 0.2 mm). The colour bar represents the soil saturation degree ($\tilde{\theta}$) when each water cluster was invaded; blue are the first and red are the last invaded clusters. **(b)** Air (white) and water (blue) distribution in the soil matrix (soil grains in grey) for $\tilde{\theta} = 0.4$ from the same run of the invasion–percolation algorithm as in (a). The magnified inset shows the formation of small water patches, which are held by capillary forces.

Extended Data Table 1: **Parameters for the two-dimensional pore-scale simulations of Fig. 2a**.

Parameters that depended on temperature (i.e, diffusion coefficients (D_i), Henry's constant (kH) and maximum reaction rate (V_m)) were calculated based on 25 °C.

Parameter	Units	Value	Description	Source
$D_{\mathrm{O_2}(g)}$	$\mathrm{m^2\ s^{-1}}$	1.9×10^{-5}	Atmospheric oxygen diffusion coefficient	[57]
$D_{\mathrm{CO_2}(g)}$	$\mathrm{m^2\ s^{-1}}$	1.4×10^{-5}	Atmospheric carbon dioxide diffusion coefficient	[57]
$D_{\mathrm{O_2}(aq)}$	$\mathrm{m^2\ s^{-1}}$	2.5×10^{-9}	Dissolved oxygen diffusion coefficient	[57]
$D_{\mathrm{CO_2}(aq)}$	$\mathrm{m^2\ s^{-1}}$	2.1×10^{-9}	Dissolved carbon dioxide diffusion coefficient	[57]
$D_{\mathrm{DOC}(aq)}$	$\mathrm{m^2\ s^{-1}}$	4.5×10^{-10}	Dissolved organic carbon diffusion coefficient	[58]
kH	$\mathrm{mol\ L^{-1}\ atm^{-1}}$	0.0013	Henry's law constant	
$C0_{O_2(g)}$	$\mathrm{mol\ m^{-3}}$	10	Representative atmospheric oxygen concentration	
$C0_{O_2(aq)}$	$\mathrm{mol\ m^{-3}}$	1.32	Dissolved oxygen concentration at the gas–liquid interface	
$C0_{DOC}$	$\mathrm{mg\ L^{-1}}$	30 ±(10)	Dissolved organic carbon concentration at the soil grain perimeter	[30]
V_m	$\mathrm{mol\ m^{-2}\ s^{-1}}$	6×10^{-12}	Maximum (surface) reaction rate	[48, 49]
$K_{m(s)}$	$\mathrm{mol\ m^{-3}}$	1 ±0.025	Michaelis constant for dissolved organic carbon	[48, 49]
$K_m(O_2)$	$\mathrm{mol\ m^{-3}}$	0.1 ±(0.05)	Michaelis constant for oxygen	[59]

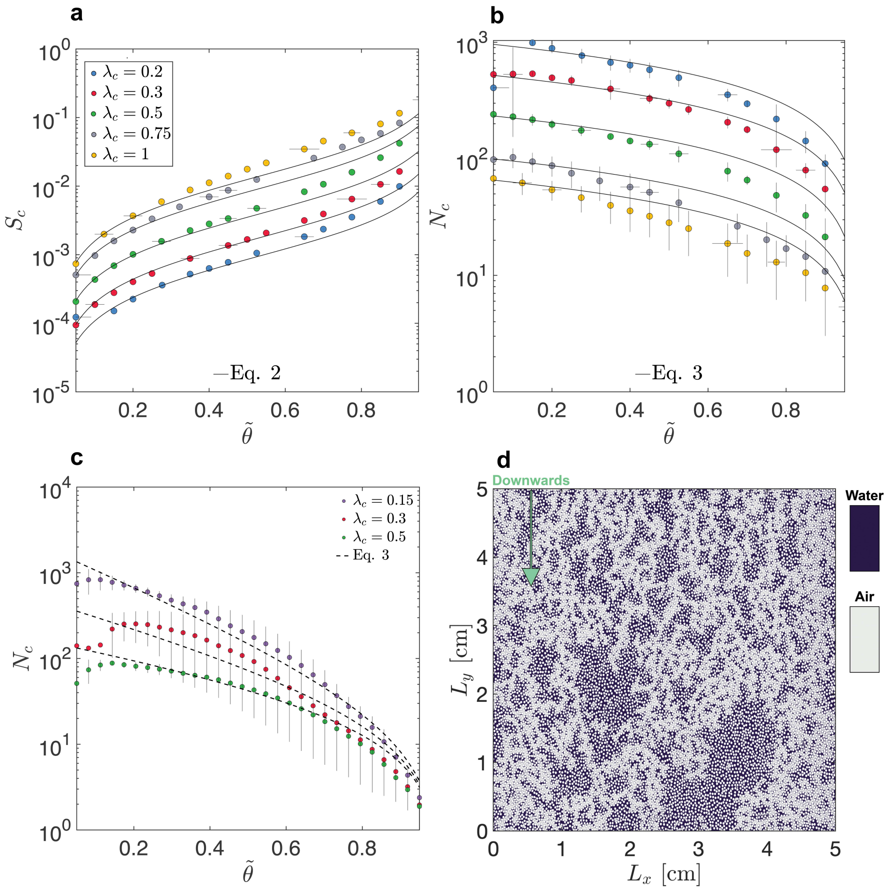

Extended Data Fig. 2: **(a)** Number and **(b)** characteristic size of water patches from the pore-scale simulations (Fig. 2a) for different grain sizes (legend). The solid lines in a and b represent Eq. 2 and Eq. 3, respectively. **(c)** Experimental measures of drainage in microfluidic chips of different grain sizes (legend) and the comparison with the scaling law of Eq. 3 (dashed lines). The vertical error bars show the standard deviation between three replicates. **(d)** A snapshot from the drainage process inside the microfluidic chip, at $\tilde{\theta} = 0.5$ ($\lambda_c = 0.15$ mm); water in blue and air in grey. Based on these images, we extracted the water patch properties (i.e., S_c and N_c).

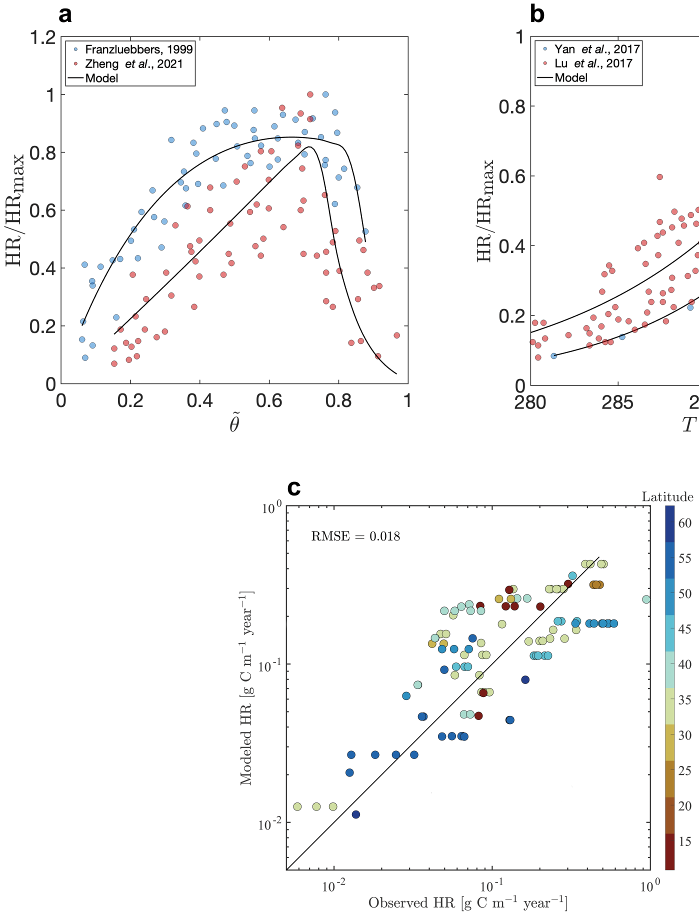

Extended Data Fig. 3: Observations (dots) of soil heterotrophic respiration as a function of **(a)** soil saturation [55, 56] and **(b)** ambient temperature [24, 25] conditions, and the predictions of our model (solid lines), based on the reported soil texture, saturation degree and ambient temperature; dissolved organic carbon concentration was assumed to be at saturated conditions (i.e., $\frac{C_s}{C_s+K_{m(s)}} \to 1$ in Eq. 5, Methods). **(c)** Model predictions plotted against field observations [27] of soil heterotrophic respiration, at different climatic locations (colour bar indicates the latitude). The respiration rate was normalized based on the reported soil depth (thus, in units of gC m^{-1} yr^{-1}).

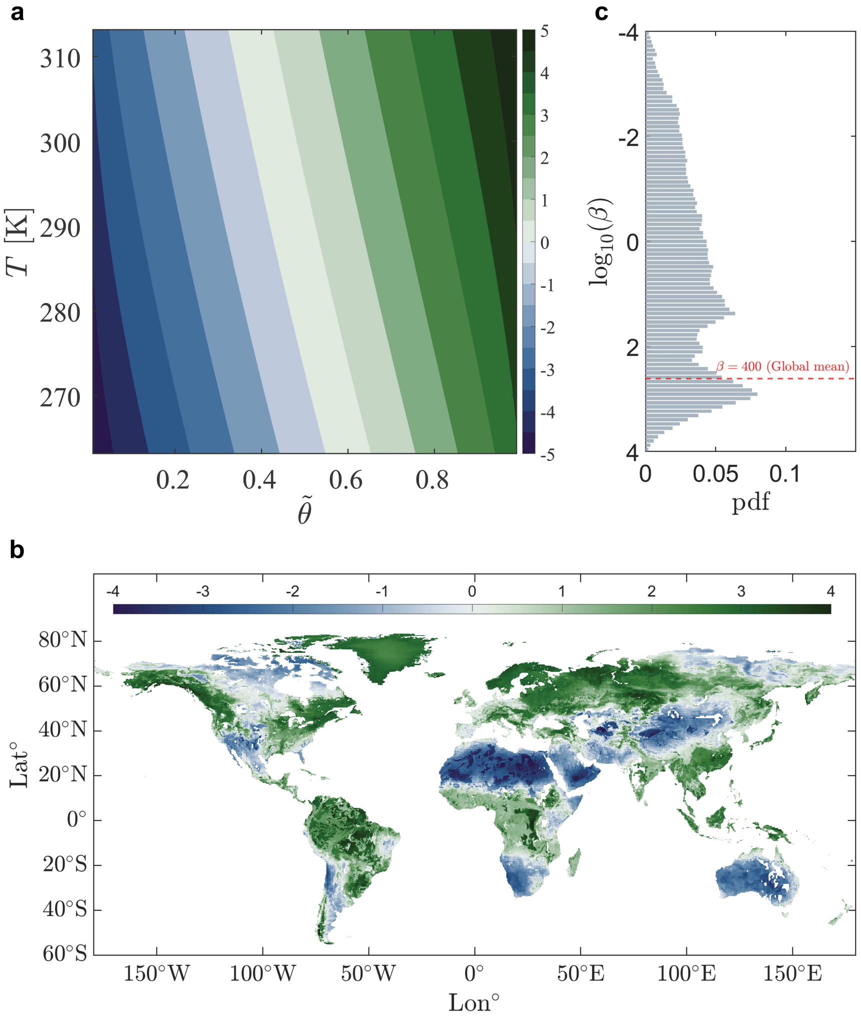

Extended Data Fig. 4: **(a)** Two-dimensional contour surface (colour scale) based on the model (Methods Eqs. 1 - 3) of $\log_{10}(\beta)$ as a function of the surface temperature (T) and soil saturation ($\tilde{\theta}$). Note that for this particular example, the global mean grain size (0.3 mm) was used to parameterize λ_c, and dissolved organic carbon concentration was assumed to be at saturated conditions (i.e., $\frac{C_s}{C_s+K_{m(s)}} \rightarrow 1$ in Eq. 5, Methods). **(b)** Global map of the annual mean β values (year 2021); colour bar on logarithmic scale ($\log_{10}(\beta)$). **(c)** Probability density function of logarithmic β values based on the global map in **b**; the overall mean value of β is $\sim$ 400 (dashed red line).

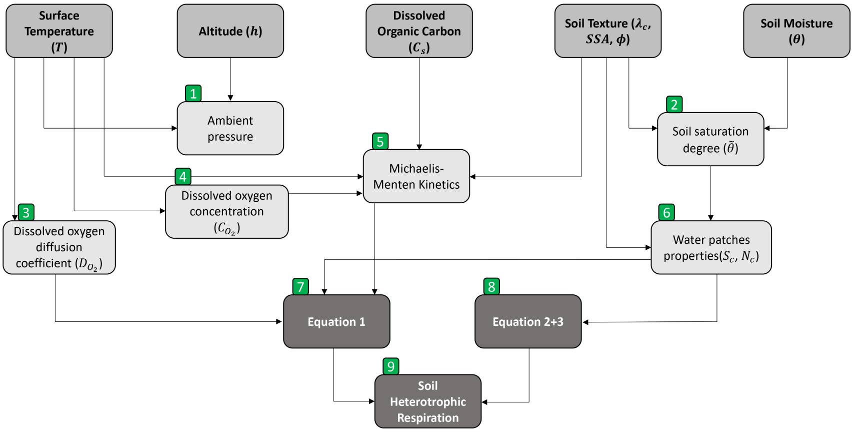

Extended Data Fig. 5:
Schematic illustration of the model methodology to derive estimates of heterotrophic respiration from climatic and soil data.
(1) Based on the altitude (h) and the ambient temperature (T), the ambient pressure is determined via the ideal gas law.
(2) Soil relative saturation degree ($\tilde{\theta}$) is calculated using the soil moisture (θ) at the topsoil layer and the porosity (ϕ), $\tilde{\theta} = \theta/\phi$.
(3): The dissolved oxygen diffusion coefficient (D_{O_2} [cm^2 s^{-1}]) in water is evaluated using an empirical relation with the ambient temperature (T) [50]: $\log_{10}(D_{\mathrm{O}_2}) = -4.41 + (773.8/T) - (506/T)^2$.
(4) Dissolved oxygen concentration is calculated using the ambient pressure (1) and Henry's law solubility parameter (kH [mol kg^{-1} bar^{-1}]). [47].
(5) Within the Michaelis–Menten kinetic [46, 48], $V_m \frac{C_s}{C_s+K_{m(s)}} \frac{C_{O_2}}{C_{O_2}+K_{m(O_2)}}$, the value of C_s is evaluated based on a dissolved organic database [30]. The maximum reaction rate is given by $V_m = \alpha_s \exp(-E_a/(RT))$; where R is the universal gas constant, T is the surface temperature, and α_s and E_a are the pre-exponential factor and activation energy of the enzymatic reaction, respectively. In the model, the value of the pre-exponential factor, α_s, is proportional to the soil surface area (SSA). Therefore, V_m, in the upscaled model, is a function of the surface temperature and the soil texture (i.e., surface area).
(6) The water patch characteristic properties, namely number (N_c, Eq. 3) and size (S_c, Eq. 2) are evaluated based on the characteristic grain size (λ_c) and the soil saturation degree ($\tilde{\theta}$).
(7) By combining the results from (3), (5) and (6), Eq. 1 can be solved (see main text).
(8) Based on the water patch properties in the system, Eqs. 2 and 3 can be solved to characterize the spatial distribution of water at different saturation conditions.
(9) By multiplying the solution of (7), i.e., the heterotrophic respiration rate for a single water patch, by the number of patches in the domain (8), we can obtain the heterotrophic respiration rate from the soil matrix (of length scale L).

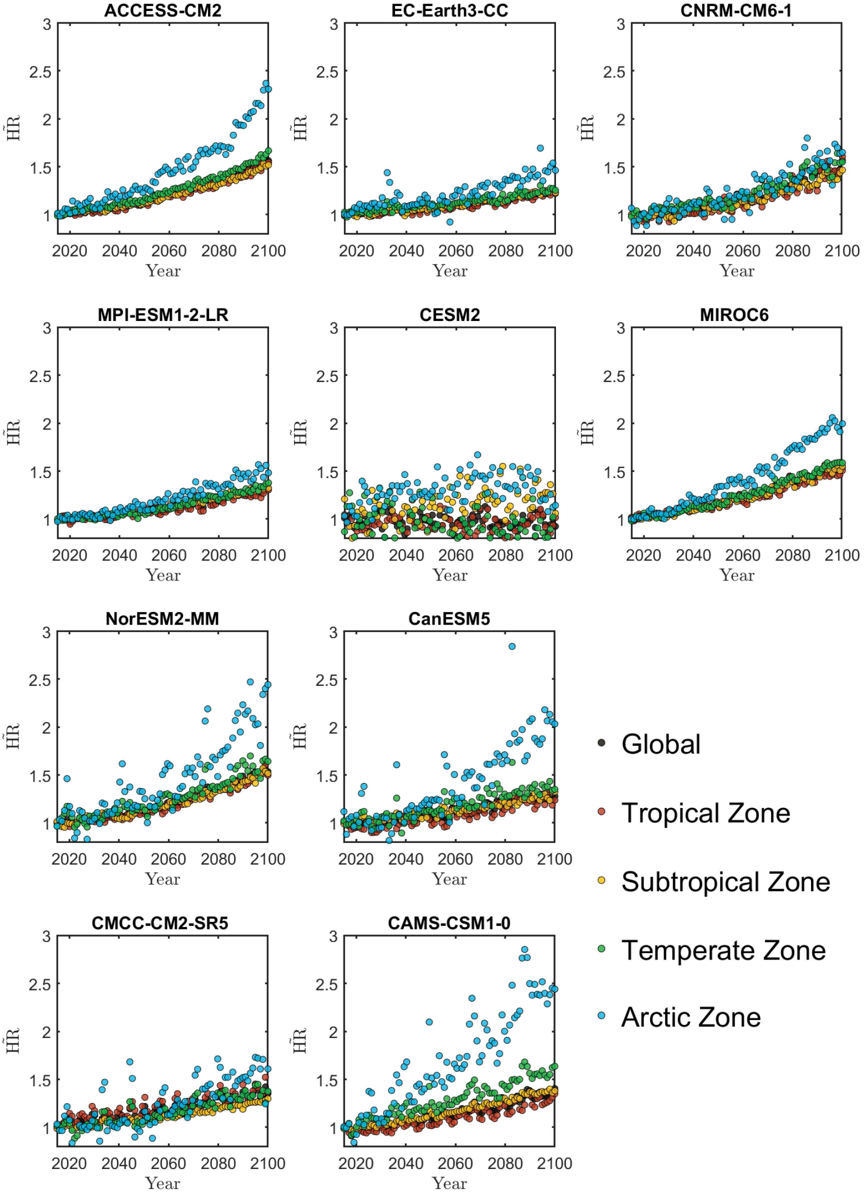

Extended Data Fig. 6: Projected changes in soil HR (ratio relative to the reference year of 2015) through the 21st century estimated using climate projections from 10 different climate models. Symbol colours represent different climate zones.

Supplementary Files

This is a list of supplementary files associated with this preprint. Click to download.

- SIPercolation.png
- SImicroFluidic.png
- figvalidation2.png
- SIbetaMap.png
- FlowChart.png
- SIEarthSM.png